

N-doped ordered mesoporous carbon prepared by solid–solid grinding for supercapacitors

Juan Du, Ran Liu, Yifeng Yu, and Yue Zhang

College of Chemical and Pharmaceutical Engineering, Hebei University of Science and Technology, Shijiazhuang 050018, China

Yixin Zhang^{a)}

Ningbo Institute of Materials Technology & Engineering, Chinese Academy of Sciences, Ningbo 315201, China

Aibing Chen^{b)}

College of Chemical and Pharmaceutical Engineering, Hebei University of Science and Technology, Shijiazhuang 050018, China

(Received 29 March 2018; accepted 13 June 2018)

N-doped ordered mesoporous carbon (N-OMC) has been one of the most promising choices as the electrode for supercapacitors due to its large surface area and uniform mesoporous structure. However, there is still a big challenge to prepare N-OMC using a relatively simple method. Here, a straightforward preparation of N-OMC was reported in which the precursor zeoliticimidazolate framework was *in situ* grown in the SBA-15 template by a fast, solvent-free, and atom economic solid–solid grinding strategy. After pyrolysis and removing of the template, the N-OMC was obtained with ordered mesoporous structure, rich oxygen and nitrogen, and a large specific surface area of 1004 m²/g. As the electrode material for supercapacitors, N-OMC displayed an excellent specific capacitance of 228 F/g at 0.2 A/g and superb charge/discharge cycling stability, which is promising for high-performance energy storage. This solid–solid grinding strategy may offer a low-cost and scalable method to produce high-performance N-OMC for the electrode from the zeoliticimidazolate framework.

I. INTRODUCTION

The rapid increase in world population and economic expansion around the world have led to increasing use of energy-based appliances, which eventually results in high energy consumption.¹ Owing to their high power density and superior cyclability relative to batteries, supercapacitors have emerged as an important electrical energy storage technology that will play a critical role in the large-scale deployment of intermittent renewable energy sources, smart power grids, and electrical vehicles. Ordered mesoporous carbon (OMC) has received considerable attention as electrode materials for fuel cells, batteries, and supercapacitors² owing to its large specific surface area, tunable pore structure, uniform and adjustable pore size, and favorable physicochemical properties such as electrical conductivity and mechanical stability.^{3–5} The ordered mesoporous structure of porous carbon plays an important role in electrochemical performances^{6–8} and allows more facile molecular transport of reactants and products thanks to its uniform channels.^{9–11} Among various synthesis strategies to develop OMC, the hard

template methods have been used generally to produce OMC with controllable morphology and tunable porous structure, in which assembling of carbon precursors in hard template channels by infiltration or polymerization is the key process.^{12–15} During the assembling process, the precursor is normally dissolved in solvent (water, ethanol, or other organics) before being evenly adsorbed in hard template channels by capillary power. A large amount of organic solvent is consumed in this strategy, leading to pollutions to the environment. It is an arduous task to recycle the organic solvent, especially in scale-up production. An environmentally friendly alternate is free-solvent strategy, more specifically, chemical vapor deposition (CVD) and solid–solid grinding method. In the conventional CVD strategy, the silica template is modified with metal or metallic oxide in advance via impregnation, then precursor gases deposit on the template in a special instrument.^{16–18} Comparatively, solid–solid grinding is easy to operate and scale-up.^{19–21} In addition, grinding can generate heat that is helpful for guest molecules including carbon precursors and metal to disperse in the template by capillary forces, which is also an energy-consuming process.^{22–25} But the capacitance properties of OMC prepared by the grinding method are relatively poor due to its inert surface property, limiting its application in supercapacitors. Doping with heteroatoms,

Address all correspondence to these authors.

^{a)}e-mail: zhangyixin@nimte.ac.cn

^{b)}e-mail: chen_ab@163.com

DOI: 10.1557/jmr.2018.219

such as oxygen and nitrogen, has been applied to improve the overall specific capacitance by providing pseudocapacitance for the supercapacitor. Many reports have demonstrated that N-doped carbons are promising for enhanced electronic double layer capacitor (EDLC) capacitance.^{15,26}

Therefore, to develop N-doped OMC is significant for supercapacitor application. To date, there are two primary strategies to develop N-doped carbon materials including post-treatment of carbons and *in situ* synthesis. In contrast to the former, *in situ* synthesis is more advantageous to form homogeneous carbon with high nitrogen content.²⁷ Recently, metal–organic frameworks such as zeoliticimidazolate frameworks (ZIFs) have been used as templates/precursors to prepare N-doped porous carbons through thermal conversion^{28,29} taking advantage of their diverse structural topologies, tunable functionalities for versatile applications. However, the N-doped porous carbons derived from ZIFs usually have low specific surface area and large micropores.³⁰ It is still a challenge to obtain OMC from ZIFs as the carbon precursor.

Herein, we reported a straightforward preparation of N-doped ordered mesoporous carbon (N-OMC) with *in situ* growth of ZIF-67 in SBA-15 by solid–solid grinding. ZIF-67 was used as carbon and nitrogen precursors, which enable the formation of the carbon matrix and introduction of nitrogen achieved simultaneously. SBA-15 was used as the template to control the mesoporous structure. Solid–solid grinding provides a solvent-free condition, which is environmentally friendly. The N-OMC with high specific surface area and ordered mesoporous characteristics showed excellent performance for supercapacitors with a specific capacitance of 228 F/g at 0.2 A/g and remarkable stability of 99.97% after 10,000 cycles at 5 A/g.

II. EXPERIMENTAL SECTION

A. Preparation of N-OMC

SBA-15 was prepared according to our previous work.³¹ Typically, 4.0 g of Pluronic P123 was dissolved in 50 mL of water and stirred for 5 h at room temperature. The mixture was added to 120 mL of 2 M hydrochloric acid solution and remained for 2 h. Then, 8.5 g of TEOS was added to that solution and stirred for 24 h at 35 °C. The mixture was then aged at 80 °C for 24 h without stirring. After completion of the reaction, the solid products were filtered, washed with deionized water, and air-dried overnight. The P123 was removed through calcining in air at 550 °C for 5 h.

The N-OMC was prepared via the template method using SBA-15 as the template and ZIF-67 as carbon and nitrogen precursors. Typically, 0.5 g SBA-15 and 0.06 g Co(NO₃)₂·6H₂O were mixed by grinding for 20 min in an agate mortar. Subsequently, 0.8 g 2-methylimidazole (Hmim) was added into the composites of Co(NO₃)₂·6H₂O and SBA-15 for another 20 min under

grinding. Finally, the ZIF-67/SBA-15 composite was carbonized by heat treatment at 750 °C in N₂. The N-OMC was obtained after etching the template and Co species.

B. Preparation of ZIF-67-S and ZIF-67-G

As reference samples, ZIF-67 was prepared in the solvent of methanol and ethanol as previously reported and solvent-free method (denoted as ZIF-67-S and ZIF-67-G) respectively. Typically, after 0.06 g Co(NO₃)₂·6H₂O and 0.8 g 2-methylimidazole were grinded in an agate mortar for about 20 min, the ZIF-67-G was obtained. Finally, the as-prepared ZIF-67-S was carbonized by heat treatment at 750 °C in N₂. The porous carbon was obtained after etching Co species as the reference sample for electrochemical performance.

C. Characterization

X-ray diffraction (XRD) patterns were achieved using a Rigaku D/MAX-2500 system (Rigaku Corporation, Tokyo, Japan) with Cu K α (λ_{ra} , 15,406 nm). Raman measurements were performed on a Jobin-Yvon HR800 spectrometer (HORIBA JobinYvon, Paris, France) using a 532 nm laser. The morphology and microstructure of samples were investigated by transmission electron microscopy (TEM; JEOL JEM-2100, JEOL, Tokyo, Japan). Nitrogen adsorption–desorption isotherms were carried out on a Micromeritics TriStar 3020 instrument (TriStar, Atlanta, Georgia) at –196 °C. The Brunauer–Emmett–Teller method was used to calculate the specific surface area, while the Barrett–Joyner–Halenda method was applied to analyze the pore size distribution using the desorption branch of isotherm. The total pore volume was obtained from the amount of N₂ adsorbed at the relative pressure ($P/P_0 = 0.97$). X-ray photoelectron spectroscopy (XPS) was conducted on a Thermo Scientific ESCALab 250Xi system (Thermo Fisher Scientific, Waltham, Massachusetts) using an Al-K α radiation under a vacuum of 3×10^{-10} mbar. Thermogravimetric analysis (Pyris 1 TGA, PerkinElmer, Waltham, Massachusetts) was performed under air flow from 20 to 800 °C at a heating rate of 10 °C/min. Fourier transform infrared (FT-IR) spectroscopy was recorded on a Nicolet 6700 FT-IR Spectrometric Analyzer (Nicolet, Madison, Wisconsin) using KBr pellets.

D. Electrochemical measurements

The working electrode was prepared by coating the viscous slurry (samples, carbon black and polytetrafluoroethylene with the mass ratio of 8:1:1 in ethanol) onto a Ni foam current collector. The mass of active material loaded on each working electrode was 4–5 mg after drying at 100 °C for 24 h. Electrochemical measurements were carried out in both three-electrode and two-electrode systems using an electrochemical

workstation (CHI 760E, Chenhua Instruments, Shanghai, China) with 6 M KOH solution as the electrolyte. For the three-electrode system, Pt wire and Hg/HgO were used as the counter and reference electrodes. For the fabrication of supercapacitor devices, two slices of electrodes were immersed in 6 M KOH and were separated by a filtration paper, then tested by the current collector. Electrochemical performances were evaluated by cyclic voltammetry (CV), galvanostatic charge–discharge (GCD), and electrical impedance spectroscopy (EIS) analysis. For the two-electrode system, the specific capacitances (C , F/g), energy density (E , W h/kg), and power density (P , W/kg) were calculated by the following equations: $C = 4I\Delta t/\Delta Vm$, $E = 0.5 C (\Delta V)^2$, and $P = E/\Delta t$, where I (A), Δt (s), ΔV (V), and m (g) are GCD current, discharge time, voltage window, and mass of the active material, respectively. In the three-electrode system, the specific gravimetric capacitance according to the GCD measurements: $C = I\Delta t/\Delta Vm$.

III. RESULTS AND DISCUSSION

The fabrication process of N-OMC is illustrated in Fig. 1. SBA-15 is a good host template due to its highly ordered hexagonal mesoporous structure and abundant silicon hydroxyl group.^{23,24,32,33} The guest molecules including metal oxides and precursors can enter the channels of mesopores of SBA-15 by solid–solid grinding. First, SBA-15 [Fig. S1(a)] and $\text{Co}(\text{NO}_3)_2 \cdot 6\text{H}_2\text{O}$ powders were mixed by grinding. As shown in Fig. S1(b), the color of mixture was changed to light pink gradually. In this process, the Si–OH group on SBA-15 can interact with Co^{2+} forming $\text{Co}-\text{O}-\text{Si}$,³³ favoring the infiltration of the guest precursor into the pores.²⁴ Second, a certain amount of Hmim was added into the composites of $\text{Co}(\text{NO}_3)_2 \cdot 6\text{H}_2\text{O}$ and SBA-15 and the mixture was ground. Hmim and $\text{Co}(\text{NO}_3)_2 \cdot 6\text{H}_2\text{O}$ could react to form ZIF-67 by grinding. After grinding, the color of the mixture turned light purple, and uniform ZIF-67/SBA-15 was obtained [Fig. S1(c)]. Subsequently, the composite of ZIF-67/SBA-15 was carbonized by heat treatment at 750 °C in N_2 .

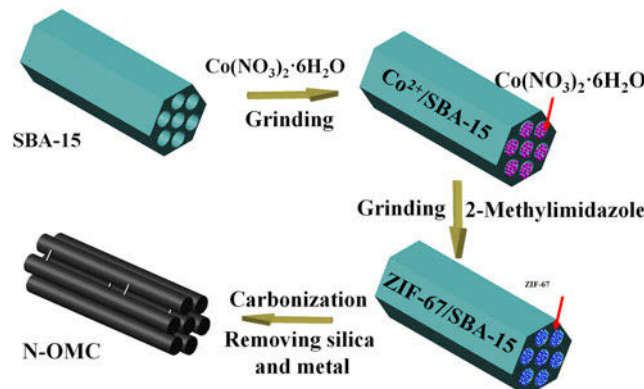


FIG. 1. Schematic of the fabrication processes of N-OMC.

Therein, ZIF-67 was pyrolyzed into nitrogen-doped carbon. Under catalysis of Co, the carbon was partially graphitized.^{1,34} Finally, black powder of N-OMC copying the morphology and porous structure of SBA-15 was obtained after etching the template and Co species [Fig. S1(d)]. This strategy presented a meaningful simple and scalable route to produce OMC materials. The operation was simple, and no organic solvent was required; furthermore, nitrogen was in situ introduced from a single nitrogen/carbon precursor.

For comparison, two pure ZIF-67 samples without SBA-15 as the template were also obtained, one was prepared by the grinding method (denoted as ZIF-67-G) and the other was prepared by the traditional solution reaction reported elsewhere (denoted as ZIF-67-S).¹² The FT-IR spectra of both samples were similar as shown in Fig. S2(a). The peak at 1584 cm^{-1} was corresponding to the C=N stretching mode of Hmim, and the peaks at 2929 and 3138 cm^{-1} were, respectively, attributed to the C–H stretching mode of aromatic ring and aliphatic chain in Hmim [Fig. S2(a)], agreeing with the reported spectrum of ZIF-67.^{35–38} The peaks at 1584 and 3138 cm^{-1} were also observed in the FTIR spectrum of ZIF-67/SBA-15, with four major bands of SBA-15 including the Si–O–Si vibrational modes at 807 and 1080 cm^{-1} , and $\text{R}^+ = \text{H}^+$ in the calcined state (962 cm^{-1}) as well as physisorbed water at 1630 cm^{-1} .³⁹

In the small angle XRD patterns of SBA-15 and ZIF-67/SBA-15 composites [Fig. S2(b)], the peaks at 0.98, 1.68, and 1.90° can be indexed to (100), (110), and (200), indicating the highly ordered hexagonal mesoporous symmetry. However, comparing with SBA-15, the peak-shift toward higher 2θ values and the weaker peak of (100) for the ZIF-67/SBA-15 composite implied that the degree of long-range structural order of SBA-15 was reduced.^{19,32,40} In the wide-angle XRD patterns [Fig. S2(c)], all the diffraction peaks of the ZIF-67-G in the 2θ range of 5–40° were matched with those reported for ZIF-67.^{28,41} By contrast, the ZIF-67/SBA-15 composite only showed wide peak and weak characteristic peaks of ZIF-67 such as 5.7, 12.2, 23.3, 29.6, and 36.3° [the arrows in Fig. S2(c)], suggesting the high dispersion of ZIF-67 nanoparticles in pores of SBA-15.²⁴ The results suggested that ZIF-67 could be prepared and dispersed into the template channels by solid–solid grinding.

The TGA analysis in N_2 was tested to illustrate the carbon residual of Hmim, ZIF-67-G, and ZIF-67/SBA-15 composite [Fig. S2(d)]. It can be seen that Hmim evaporated completely above 200 °C. For ZIF-67-G, the mass loss in 150–200 °C was correlated with water evaporation,⁴² and the mass loss in 500–600 °C was the thermal characteristics of ZIF-67.^{43,44} ZIF-67/SBA-15 composites had a similar TGA weight-loss curve with ZIF-67-G. But ZIF-67/SBA-15 composites showed higher loss temperatures of 182 and 633 °C than

ZIF-67-G (145 and 520 °C), suggesting that pyrolysis of ZIF-67 occurred at higher temperatures in the confined nanospace of SBA-15.⁴⁵

After carbonization in N₂, the ZIF-67 in SBA-15 converted into N-doped carbon. In comparison with SBA-15 and ZIF-67/SBA-15, the small angle XRD of N-OMC [Fig. 2(a)] only exhibited a obvious diffraction peak at $2\theta = 0.98^\circ$, which reveals that N-OMC retained a relatively weak 2D hexagonal ordered mesoporous structure corresponding to *P6mm* space group of SBA-15 after etching silica and metal. The wide-angle XRD patterns of N-OMC, as depicted in Fig. 2(b), clearly showed two wide peaks at 26.0 and 44.0° [the sign inset of Fig. 2(b)], which are assigned to the diffractions of (002) and (100) planes of graphite carbon (JCPDS No. 75-1621), indicating an insufficient graphitization catalyzed by Co species.

The Raman characterization of N-OMC was analyzed to reveal the lattice disordering in carbon materials, as illustrated in Fig. 2(c). The Raman spectrum of the N-OMC showed characteristic D and G bands at 1320 and 1580 cm⁻¹, which are associated with the disordered carbon atoms and *sp*² hybridized graphitic carbon atoms, respectively.⁴⁴ The intensity ratio (I_D/I_G) of 1.00 confirmed the layered structure with a disordered graphitic lattice,⁴⁶ agreeing with the result of wide-angle XRD.

Nitrogen isothermal adsorption–desorption measurements were performed to analyze the textural properties

of the N-OMC. As depicted in Fig. 2(d), a type IV adsorption–desorption isotherm and H3 hysteresis loop were observed. A sharp increase at low relative pressure ($P/P_0 < 0.1$) was observed, revealing the abundant micropores in the samples.⁴⁷ Moreover, the hysteresis at relative higher pressure ($P/P_0 > 0.4$) indicated the presence of mesopores.^{48–50} In addition, N-OMC had a specific surface area of 1006 m²/g and a pore volume of 0.96 cm³/g. It is worth noticing that the specific surface area of the N-OMC was higher than those of the reported mesoporous carbon^{51,52} and the porous carbon with less mesoporous structure (235 m²/g) obtained by carbonization of ZIF-67-S (Fig. S3). The high specific surface area favors high performance in supercapacitor due to more reaction sites.⁵³ The pore size distribution of N-OMC from the adsorption branch displayed uniform pore size distribution at 3.6 nm in the inset of Fig. 2(d), which was close to the wall thickness (4 nm) of the SBA-15 template, suggesting that mesopores were formed by the removal of the template.

The morphology and porous structure of N-OMC was studied by SEM and TEM. SEM images of N-OMC are shown in Figs. 3(a) and 3(b). The small rod-like subparticles were 1–2 μm in length and 0.5 μm in diameter. The TEM images of Fig. 3(c) display a rod-like morphology and relatively ordered mesoporous structure. From the magnification TEM images [Fig. 3(d)], it could be seen that the sample consisted of ordered arrays of

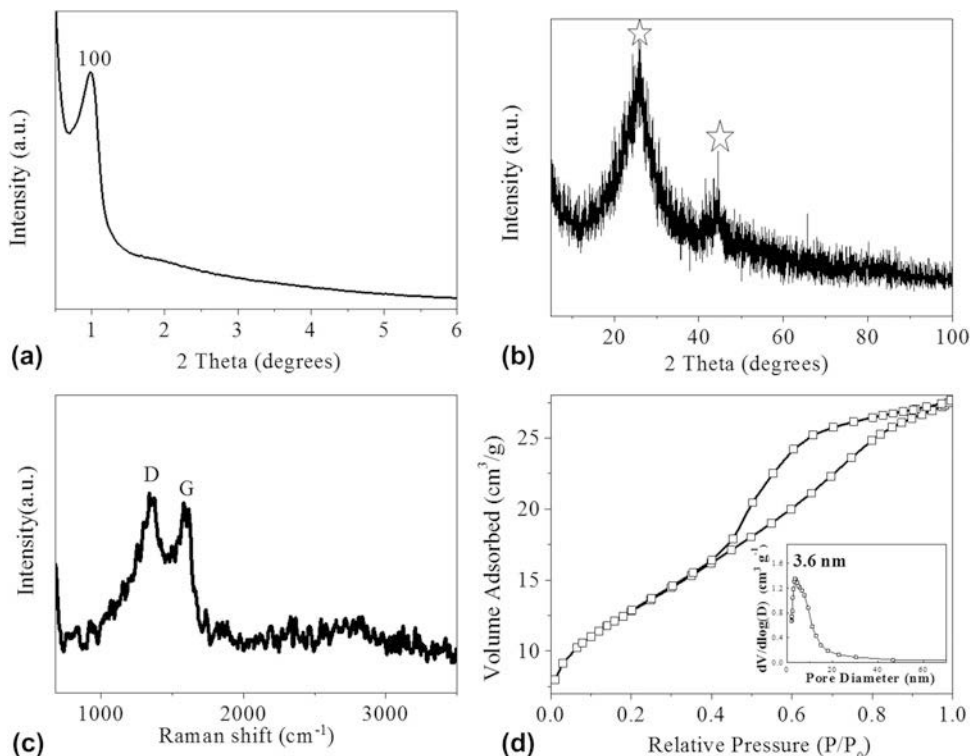


FIG. 2. Small and wide-angle XRD patterns (a and b), Raman spectrum (c), and nitrogen isothermal adsorption–desorption (d) of N-OMC.

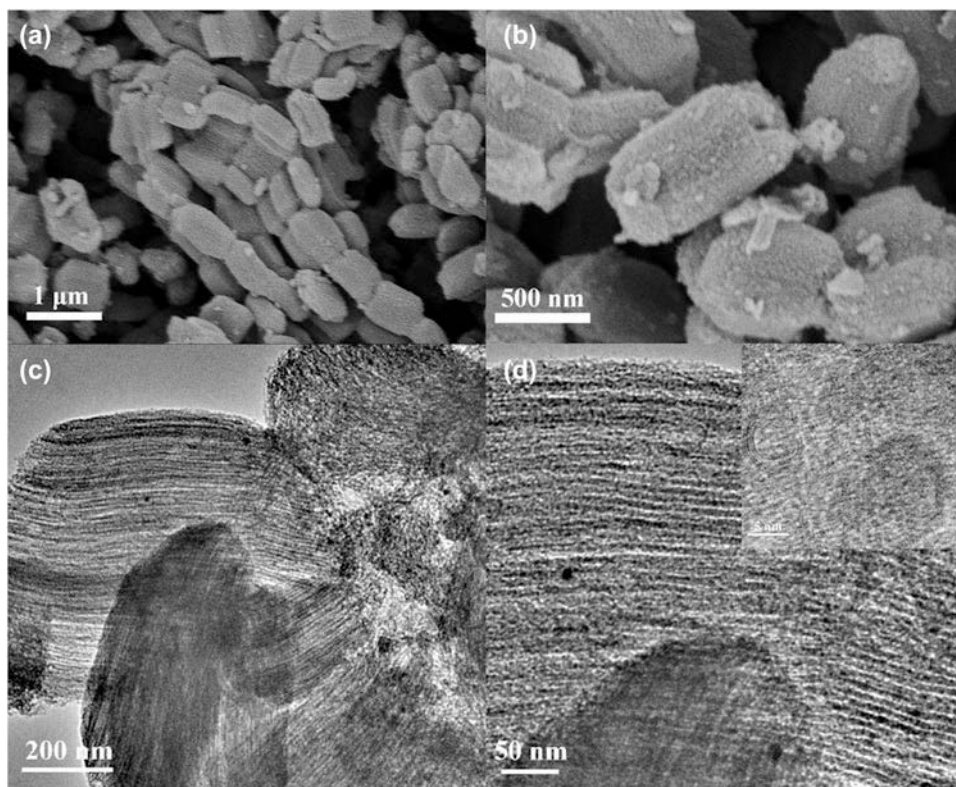


FIG. 3. SEM (a and b) and TEM images (c and d) and high resolution TEM image (inset) of N-OMC.

mesopores with one-dimensional channels, in agreement with the results of small angle XRD. The mesoporous structure of N-OMC with a uniform size of 3.6 nm could be seen from the TEM images, consistent with the wall thickness of the SBA-15 template and pore size distribution. Moreover, some carbon with disorder pores could also be seen (Fig. S4), accounting for ZIF-67 generated on the surface of SBA-15. The graphitic structure was seen in the TEM images of the N-OMC [Fig. 3(d) inset], which was attributed to the catalytic graphitization at high temperature. The lattice distance of graphite was 0.34 nm, agreeing well with the (002) plane of the graphitic sheet.

Surface chemistry of the N-OMC was investigated by XPS to provide quantitative and qualitative information of the surface elemental composition and its chemical environments. As shown in Fig. 4(a), the survey curve presented three dominated peaks centering at 284.6, 531.6, and 399.6 eV, corresponding to C1s, O1s, and N1s, respectively. Thereby, the atomic contents of C, O, and N were, respectively, estimated to be 84.55%, 6.00%, and 9.45%, suggesting an effective carbonization and high nitrogen doping. The high resolution XPS spectra of C1s, O1s, and N1s were collected to demonstrate the formed C–C, O–C, and N–C bonding. As depicted in Fig. 4(b), the C1s core-level spectrum was divided to two peaks centering at 284.6 and 285.9 eV, respectively,

being ascribed to the primary C–C/C=C carbon bonds, residual C–O bonds, and C=O bonds formed in the pyrolysis process of the carbon precursor.⁵⁴ The oxygen functionalities by deconvolution of the O1s peaks [Fig. 4(c)] were the carboxyl C=O bonds centering at 531.6 eV, and hydroxyl oxygen in amorphous hydrogenated carbon at 532.8 eV, respectively.⁵⁵ The deconvolution of the core-level N1s spectrum identified two nitrogen-containing species [Fig. 4(d)], i.e., the pyridinic N and pyrrolic N centering at 398.5 and 400.2 eV,⁵⁶ respectively. Generally, there are four types of nitrogen in nitrogen-doped carbon materials depending on the bonding environments, including pyrrolic N (400.1–400.2 eV), pyridinic N (398.2–398.5 eV), quaternary N/graphitic N (401.1 eV), and N oxides of pyridinic N (402–405 eV), as shown in the inset of Fig. 4(d). The incorporation of nitrogen and oxygen species into the carbon framework normally increases the electron density, electron donating ability, and surface basic sites of the carbon materials.

OMC has been widely applied for the electrode in supercapacitors due to its large specific surface area, tunable pore structure, and uniform or adjustable pore size. In addition, the modification of carbon materials with nitrogen or oxygen functionalities is effective to improve the capacity while maintaining the superb cycle ability of the supercapacitor.^{57,58} High energy density (or

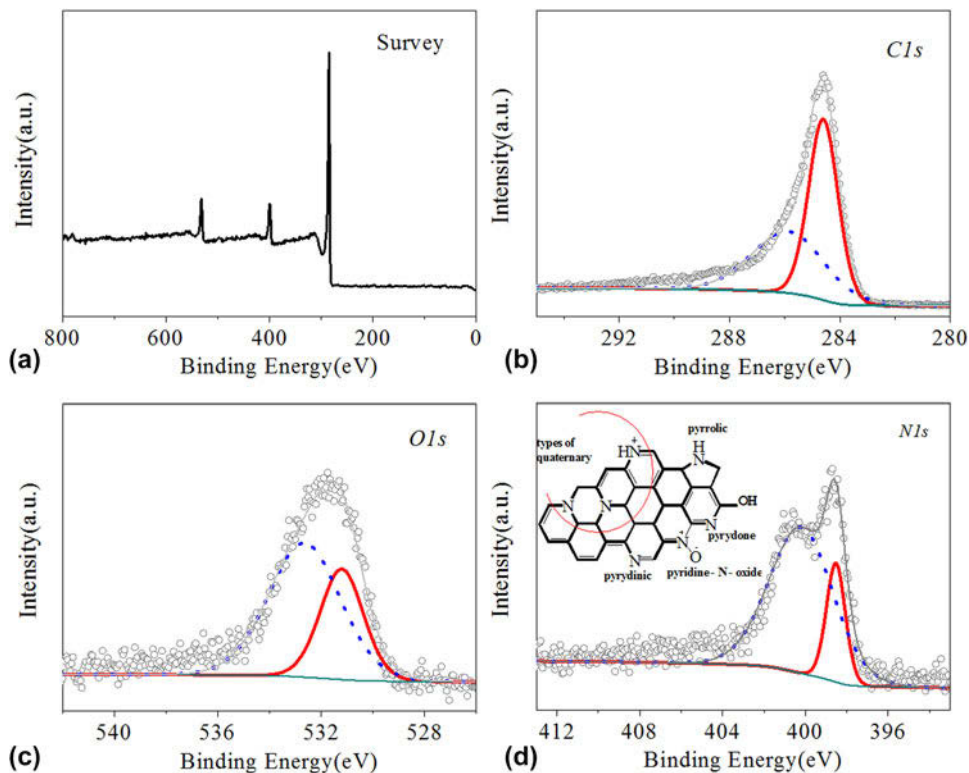


FIG. 4. XPS patterns of N-OMC (a), C1s, (b) O1s, (c) and N1s, and (d) spectrum of N-OMC.

gravimetric capacitance) at a high charge–discharge rate is required for a good electrochemical energy storage device. Thus, CV curves at different scan rates and GCD tests at different current densities for N-OMC were conducted as shown in Figs. 5(a) and 5(b). It could be seen that when the scan rate increased from 5 to 30 mV/s, a rectangular shape was retained [Fig. 5(a)], indicating a good capacitance performance at a high scan rate and an ideal EDLC.^{59,60} The current density increased with increasing of scan rate, and the CV curves showed a slight tilt rectangular-like shape especially at 100 or 200 mV/s [Fig. S5(a)], implying a fast charge/discharge process with high power capability and low equivalent series resistance. The nearly symmetric triangular-like shapes of charge–discharge curves from 0.2 to 2 A/g [Fig. 5(b)] further confirmed the electronic double-layer energy storage mechanism. As shown in Fig. S5(b), it was noted that even at a high current density of 20 A/g, the discharge curves of the N-OMC capacitor only exhibited a rather small voltage drop (IR drop) (0.31 V), suggesting a rather low internal resistance. The specific capacities calculated by discharge branches and the rate performance at the current density range of 0.2–20 A/g were shown in Fig. 5(c). The specific capacitance was calculated to be 228 F/g at the current density of 0.2 A/g, which was higher than many mesoporous carbon materials as shown in Fig. 5(c).^{49,61–70} Moreover, it can be seen that the N-OMC had a high capacitance retention over

51%, indicating that the N-OMC with a higher specific surface area provided more transport and diffusion channels for electrolyte ions.

The GCD of N-OMC and the porous carbon obtained by carbonization of ZIF-67-S were tested. As shown in Fig. S6, the GCD curves of N-OMC had a higher specific capacitance than that of porous carbon obtained by carbonization of ZIF-67-S from 0.2 to 1 A/g, consistent with the previous result of ZIF-67-S (144 F/g) as the carbon precursor for supercapacitors.³⁰ This result indicated that the ordered mesoporous structure and large specific surface area have a positive effect on electrochemical performance.

Long cycling is another crucial parameter for practical applications of supercapacitors. As displayed in Fig. 5(d), 99.97% of initial capacity was retained after 10,000 cyclic tests and the stability was better than many other mesoporous carbon materials prepared by different methods (detailed in Table SI). The GCD curves of the last 10 cycles were almost similar with the first 10 cycles [Fig. 5(d) inset], which were linear and symmetrical, indicating excellent capacitive property and long-term electrochemical stability.

The facilitated ion and electron transport behavior of N-OMC was confirmed by the EIS test before and after long cycle test. As shown in Fig. 5(e), the Nyquist plots of the N-OMC electrode consisted of capacitive semi-circles in the high frequency region and straight lines at

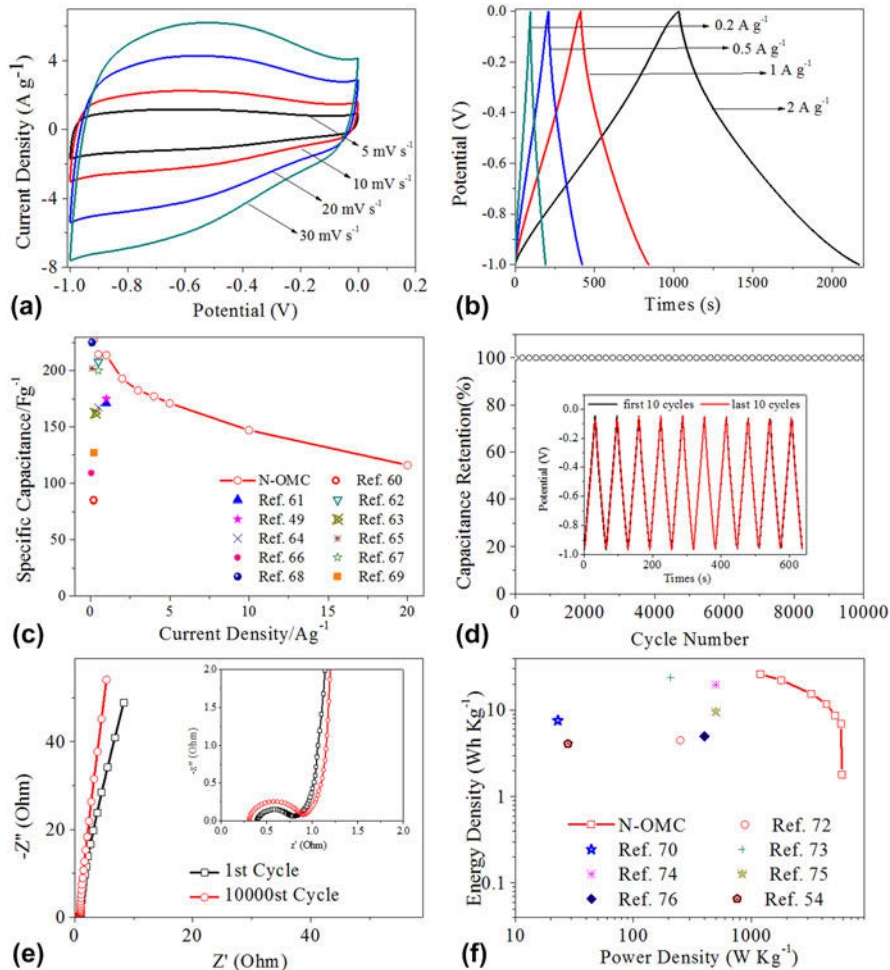


FIG. 5. Electrochemical evaluation of N-OMC: CV curves at different scan rates (a), GCD curves at different current densities (b), specific capacitances at different current densities and specific capacitances in previous studies (c), Cycle stability of the electrode at 5.0 A/g (d) and GCD curves of the first and last 10 cycles (inset), Nyquist plots with fitting curves (e) and their corresponding high frequency ranges (inset), and Ragone plots comparison with the reported porous carbons (f).

different constant inclining angles in the low-frequency region. In the low-frequency region, the Nyquist plot presented a straight line for an EDLC supercapacitor.⁷¹ At high frequency, the solution resistance (R_s) and the charge transfer resistance (R_{ct}) were obtained from the intercept at real axis and the semicircle intercepts in the Nyquist plots, which were determined to be 0.39 and 0.40 Ω , respectively, before the long cycle test. After 10,000 charge–discharge cycles, the R_s value was lowered to be 0.31 Ω . The two close R_s values and the similar semicircle before and after long cycle test showed the excellent stability of the N-OMC.

The capacitive behavior of the N-OMC sample using 6 M KOH as the aqueous electrolyte was further investigated in a two-electrode system. The CV curves of the N-OMC [Fig. S7(a)] exhibited a rectangular shape even at a rate as high as 200 mV/s. The quasi linear GCD curves at different current densities confirmed the good EDLC feature of N-OMC [Fig. S7(b)]. The specific

capacitance of the N-OMC was calculated to be 199 F/g at a current density of 0.5 A/g.

Figure 5(f) showed a Ragone plot of the corresponding power and energy densities based on the two-electrode system. N-OMC exhibited a higher specific energy density of 26.3 W h/kg surpassing most of porous carbons reported elsewhere.^{67,70,72–76} Even at a higher power density of 5885 W/kg, the specific energy density of 1.8 W h/kg was still retained. The superior performance could be attributed to the nanostructure, O and N doping as well as high specific surface area of N-OMC, confirming that the synthesized N-OMC sample was promising as an electrode material for high power supercapacitors.

IV. CONCLUSION

A fabrication of N-OMC was demonstrated by a simple approach with in situ growth of ZIF-67 in SBA-15 by

solid–solid grinding. The successful growth of ZIF-67 nanoparticles in SBA-15 was proved by FT-IR, XRD, and TGA analysis. The nitrogen/oxygen doping induced defects in the carbon framework and increased the electrochemistry performance due to good hydrophilicity of nitrogen and oxygen. The ordered mesoporous structure of ZIF-67 derived carbon favored high specific capacity. The resulting N-OMC, featuring with high specific surface area and a high amount of nitrogen and oxygen doping (9.45 and 6.00 at.%, respectively), exhibited outstanding electrochemistry performance and remarkable long-term stability of 99.97% after 10,000 cycles as electrode materials for supercapacitors. Thereby, the simple effective solid–solid grinding method will open a new direction for preparing N-OMC for supercapacitors.

ACKNOWLEDGMENTS

This work was financially supported by the National Natural Science Foundation of China (21676070), Hebei Natural Science Foundation (B2015208109), Hebei Training Program for Talent Project (A201500117), Hebei One Hundred-Excellent Innovative Talent Program (III) (SLRC2017034), Chinese Academy of Sciences (QYZDB-SSW-JSC037 and ZDRW-CN-2016-1), International Science and Technology Cooperation Program of Ningbo City (2014D10004), and Hebei Science and Technology Project (17214304D and 16214510D).

REFERENCES

- R.R. Salunkhe, J. Tang, Y. Kamachi, T. Nakato, J.H. Kim, and Y. Yamauchi: Asymmetric supercapacitors using 3D nanoporous carbon and cobalt oxide electrodes synthesized from a single metal–organic framework. *ACS Nano* **9**, 6288 (2015).
- J. Wei, D. Zhou, Z. Sun, Y. Deng, Y. Xia, and D. Zhao: A controllable synthesis of rich nitrogen-doped ordered mesoporous carbon for CO₂ capture and supercapacitors. *Adv. Funct. Mater.* **23**, 2322 (2013).
- D. Tang, S. Hu, F. Dai, R. Yi, M.L. Gordin, S. Chen, J. Song, and D. Wang: Self-templated synthesis of mesoporous carbon from carbon tetrachloride precursor for supercapacitor electrodes. *ACS Appl. Mater. Interfaces* **8**, 6779 (2016).
- J. Ma, Y. Ren, X. Zhou, L. Liu, Y. Zhu, X. Cheng, P. Xu, X. Li, Y. Deng, and D. Zhao: Pt nanoparticles sensitized ordered mesoporous WO₃ semiconductor: Gas sensing performance and mechanism study. *Adv. Funct. Mater.* **28**, 1705268 (2018).
- J. Wei, Z. Sun, W. Luo, Y. Li, A.A. Elzatahry, A.M. Al-Enizi, Y. Deng, and D. Zhao: New insight into the synthesis of large-pore ordered mesoporous materials. *J. Am. Chem. Soc.* **139**, 1706 (2017).
- W. Chen, J. Shi, T. Zhu, Q. Wang, J. Qiao, and J. Zhang: Preparation of nitrogen and sulfur dual-doped mesoporous carbon for supercapacitor electrodes with long cycle stability. *Electrochim. Acta* **177**, 327 (2015).
- T. Cai, M. Zhou, D. Ren, G. Han, and S. Guan: Highly ordered mesoporous phenol–formaldehyde carbon as supercapacitor electrode material. *J. Power Sources* **231**, 197 (2013).
- Y. Zhu, Y. Zhao, J. Ma, X. Cheng, J. Xie, P. Xu, H. Liu, H. Liu, H. Zhang, M. Wu, A.A. Elzatahry, A. Alghamdi, Y. Deng, and D. Zhao: Mesoporous tungsten oxides with crystalline framework for highly sensitive and selective detection of foodborne pathogens. *J. Am. Chem. Soc.* **139**, 10365 (2017).
- D.S. Yang, D. Bhattacharjya, S. Inamdar, J. Park, and J.S. Yu: Phosphorus-doped ordered mesoporous carbons with different lengths as efficient metal-free electrocatalysts for oxygen reduction reaction in alkaline media. *J. Am. Chem. Soc.* **134**, 16127 (2012).
- Q. Yue, Y. Zhang, Y. Jiang, J. Li, H. Zhang, C. Yu, A.A. Elzatahry, A. Alghamdi, Y. Deng, and D. Zhao: Nano-engineering of core–shell magnetic mesoporous microspheres with tunable surface roughness. *J. Am. Chem. Soc.* **139**, 4954 (2017).
- Q. Yue, J. Li, Y. Zhang, X. Cheng, X. Chen, P. Pan, J. Su, A.A. Elzatahry, A. Alghamdi, Y. Deng, and D. Zhao: Plasmolysis-inspired nanoengineering of functional yolk–shell microspheres with magnetic core and mesoporous silica shell. *J. Am. Chem. Soc.* **139**, 15486 (2017).
- Y. Hu, H. Liu, Q. Ke, and J. Wang: Effects of nitrogen doping on supercapacitor performance of a mesoporous carbon electrode produced by a hydrothermal soft-templating process. *J. Mater. Chem. A* **2**, 11753 (2014).
- J-T. Dai, Y. Zhang, H-C. Li, Y-H. Deng, A.A. Elzatahry, A. Alghamdi, D-L. Fu, Y-J. Jiang, and D-Y. Zhao: Enhancement of gemcitabine against pancreatic cancer by loading in mesoporous silica vesicles. *Chin. Chem. Lett.* **28**, 531 (2017).
- Y. Liu, Z. Wang, W. Teng, H. Zhu, J. Wang, A.A. Elzatahry, D. Al-Dahyan, W. Li, Y. Deng, and D. Zhao: A template-catalyzed in situ polymerization and co-assembly strategy for rich nitrogen-doped mesoporous carbon. *J. Mater. Chem. A* **6**, 3162 (2018).
- Z-S. Wu, X. Feng, and H-M. Cheng: Recent advances in graphene-based planar micro-supercapacitors for on-chip energy storage. *Natl. Sci. Rev.* **1**, 277 (2014).
- Y. Wang, C. Zhang, S. Kang, B. Li, Y. Wang, L. Wang, and X. Li: Simple synthesis of graphitic ordered mesoporous carbon supports using natural seed fat. *J. Mater. Chem.* **21**, 14420 (2011).
- Y. Dong, Z-S. Wu, W. Ren, H-M. Cheng, and X. Bao: Graphene: A promising 2D material for electrochemical energy storage. *Sci. Bull.* **62**, 724 (2017).
- S. Zheng, Z-S. Wu, S. Wang, H. Xiao, F. Zhou, C. Sun, X. Bao, and H-M. Cheng: Graphene-based materials for high-voltage and high-energy asymmetric supercapacitors. *Energy Storage Mater.* **6**, 70 (2017).
- Y. Wang, B. Li, C. Zhang, X. Song, H. Tao, S. Kang, and X. Li: A simple solid–liquid grinding/templating route for the synthesis of magnetic iron/graphitic mesoporous carbon composites. *Carbon* **51**, 397 (2013).
- X. Zhou, X. Cheng, Y. Zhu, A.A. Elzatahry, A. Alghamdi, Y. Deng, and D. Zhao: Ordered porous metal oxide semiconductors for gas sensing. *Chin. Chem. Lett.* **29**, 405 (2018).
- H. Xiao, Z.S. Wu, L. Chen, F. Zhou, S. Zheng, W. Ren, H.M. Cheng, and X. Bao: One-step device fabrication of phosphorene and graphene interdigital micro-supercapacitors with high energy density. *ACS Nano* **11**, 7284 (2017).
- Y. Wang, B. Li, C. Zhang, H. Tao, S. Kang, S. Jiang, and X. Li: Simple synthesis of metallic Sn nanocrystals embedded in graphitic ordered mesoporous carbon walls as superior anode materials for lithium ion batteries. *J. Power Sources* **219**, 89 (2012).
- W. Yue and W. Zong: Synthesis of porous single crystals of metal oxides via a solid–liquid route. *Chem. Mater.* **19**, 2359 (2007).
- Q. Jiang, Z.Y. Wu, Y.M. Wang, Y. Cao, C.F. Zhou, and J.H. Zhu: Fabrication of photoluminescent ZnO/SBA-15 through directly dispersing zinc nitrate into the as-prepared mesoporous silica occluded with template. *J. Mater. Chem.* **16**, 1536 (2006).

25. J. Qin, F. Zhou, H. Xiao, R. Ren, and Z.-S. Wu: Mesoporous polypyrrole-based graphene nanosheets anchoring redox polyoxometalate for all-solid-state micro-supercapacitors with enhanced volumetric capacitance. *Sci. China Mater.* **61**, 233 (2017).
26. P. Matter, L. Zhang, and U. Ozkan: The role of nanostructure in nitrogen-containing carbon catalysts for the oxygen reduction reaction. *J. Catal.* **239**, 83 (2006).
27. Y. Deng, Y. Xie, K. Zou, and X. Ji: Review on recent advances in nitrogen-doped carbons: Preparations and applications in supercapacitors. *J. Mater. Chem. A* **4**, 1144 (2016).
28. R. Wu, X. Qian, X. Rui, H. Liu, B. Yadian, K. Zhou, J. Wei, Q. Yan, X.Q. Feng, Y. Long, L. Wang, and Y. Huang: Zeolitic imidazolate framework 67-derived high symmetric porous Co_3O_4 hollow dodecahedra with highly enhanced lithium storage capability. *Small* **10**, 1932 (2014).
29. A.D. Katsenis, A. Puskaric, V. Strukil, C. Mottillo, P.A. Julien, K. Uzarevic, M.H. Pham, T.O. Do, S.A. Kimber, P. Lazic, O. Magdysyuk, R.E. Dinnebier, I. Halasz, and T. Friscic: In situ X-ray diffraction monitoring of a mechanochemical reaction reveals a unique topology metal–organic framework. *Nat. Commun.* **6**, 6662 (2015).
30. F. Wei, J. Jiang, G. Yu, and Y. Sui: A novel cobalt–carbon composite for the electrochemical supercapacitor electrode material. *Mater. Lett.* **146**, 20 (2015).
31. A. Chen, Y. Yu, R. Wang, Y. Yu, W. Zang, P. Tang, and D. Ma: Nitrogen-doped dual mesoporous carbon for the selective oxidation of ethylbenzene. *Nanoscale* **7**, 14684 (2015).
32. A. Katiyar, S. Yadav, P.G. Smirniotis, and N.G. Pinto: Synthesis of ordered large pore SBA-15 spherical particles for adsorption of biomolecules. *J. Chromatogr. A* **1122**, 13 (2006).
33. Y.M. Wang, Z.Y. Wu, L.Y. Shi, and J.H. Zhu: Rapid functionalization of mesoporous materials: Directly dispersing metal oxides into as-prepared SBA-15 occluded with template. *Adv. Mater.* **17**, 323 (2005).
34. D. Zhang, H. Shi, R. Zhang, Z. Zhang, N. Wang, J. Li, B. Yuan, H. Bai, and J. Zhang: Quick synthesis of zeolitic imidazolate framework microflowers with enhanced supercapacitor and electrocatalytic performances. *RSC Adv.* **5**, 58772 (2015).
35. K.Y. Lin and H.A. Chang: Ultra-high adsorption capacity of zeolitic imidazole framework-67 (ZIF-67) for removal of malachite green from water. *Chemosphere* **139**, 624 (2015).
36. X. Li, X. Gao, L. Ai, and J. Jiang: Mechanistic insight into the interaction and adsorption of Cr(VI) with zeolitic imidazolate framework-67 microcrystals from aqueous solution. *Chem. Eng. J.* **274**, 238 (2015).
37. K-Y.A. Lin and H-A. Chang: Zeolitic imidazole framework-67 (ZIF-67) as a heterogeneous catalyst to activate peroxymonosulfate for degradation of rhodamine B in water. *J. Taiwan Inst. Chem. Eng.* **53**, 40 (2015).
38. K-Y. Andrew Lin and W-D. Lee: Self-assembled magnetic graphene supported ZIF-67 as a recoverable and efficient adsorbent for benzotriazole. *Chem. Eng. J.* **284**, 1017 (2016).
39. Y. Park, W.S. Shin, and S-J. Choi: Ammonium salt of heteropoly acid immobilized on mesoporous silica (SBA-15): An efficient ion exchanger for cesium ion. *Chem. Eng. J.* **220**, 204 (2013).
40. A. Chen, Y. Yu, Y. Li, Y. Li, and M. Jia: Solid-state grinding synthesis of ordered mesoporous MgO/carbon spheres composites for CO_2 capture. *Mater. Lett.* **164**, 520 (2016).
41. R. Wu, D.P. Wang, J. Han, H. Liu, K. Zhou, Y. Huang, R. Xu, J. Wei, X. Chen, and Z. Chen: A general approach towards multi-faceted hollow oxide composites using zeolitic imidazolate frameworks. *Nanoscale* **7**, 965 (2015).
42. C. Long, L. Jiang, X. Wu, Y. Jiang, D. Yang, C. Wang, T. Wei, and Z. Fan: Facile synthesis of functionalized porous carbon with three-dimensional interconnected pore structure for high volumetric performance supercapacitors. *Carbon* **93**, 412 (2015).
43. J. Qian, F. Sun, and L. Qin: Hydrothermal synthesis of zeolitic imidazolate framework-67 (ZIF-67) nanocrystals. *Mater. Lett.* **82**, 220 (2012).
44. J. Yang, F. Zhang, H. Lu, X. Hong, H. Jiang, Y. Wu, and Y. Li: Hollow Zn/Co ZIF particles derived from core–shell ZIF-67@ZIF-8 as selective catalyst for the semi-hydrogenation of acetylene. *Angew. Chem., Int. Ed.* **54**, 10889 (2015).
45. Q. Sun, W.C. Li, and A.H. Lu: Insight into structure-dependent self-activation mechanism in a confined nanospace of core–shell nanocomposites. *Small* **9**, 2086 (2013).
46. K. Bazzi, K.S. Dhindsa, A. Dixit, M.B. Sahana, C. Sudakar, M. Nazri, Z. Zhou, P. Vaishnav, V.M. Naik, G.A. Nazri, and R. Naik: Nanostructured high specific capacity C-LiFePO_4 cathode material for lithium-ion batteries. *J. Mater. Res.* **27**, 424 (2011).
47. Y. Yan, Q. Cheng, G. Wang, and C. Li: Growth of polyaniline nanowhiskers on mesoporous carbon for supercapacitor application. *J. Power Sources* **196**, 7835 (2011).
48. Y. Hou, Z. Wen, S. Cui, S. Ci, S. Mao, and J. Chen: An advanced nitrogen-doped graphene/cobalt-embedded porous carbon polyhedron hybrid for efficient catalysis of oxygen reduction and water splitting. *Adv. Funct. Mater.* **25**, 872 (2015).
49. X. Zhao, Q. Zhang, C-M. Chen, B. Zhang, S. Reiche, A. Wang, T. Zhang, R. Schlögl, and D. Sheng Su: Aromatic sulfide, sulfoxide, and sulfone mediated mesoporous carbon monolith for use in supercapacitor. *Nano Energy* **1**, 624 (2012).
50. Q. Wang, J. Yan, T. Wei, J. Feng, Y. Ren, Z. Fan, M. Zhang, and X. Jing: Two-dimensional mesoporous carbon sheet-like framework material for high-rate supercapacitors. *Carbon* **60**, 481 (2013).
51. U.B. Nasini, V.G. Bairi, S.K. Ramasahayam, S.E. Bourdo, T. Viswanathan, and A.U. Shaikh: Phosphorous and nitrogen dual heteroatom doped mesoporous carbon synthesized via microwave method for supercapacitor application. *J. Power Sources* **250**, 257 (2014).
52. C-W. Huang, C-H. Hsu, P-L. Kuo, C-T. Hsieh, and H. Teng: Mesoporous carbon spheres grafted with carbon nanofibers for high-rate electric double layer capacitors. *Carbon* **49**, 895 (2011).
53. H.L. Jiang, B. Liu, Y.Q. Lan, K. Kuratani, T. Akita, H. Shioyama, F. Zong, and Q. Xu: From metal–organic framework to nanoporous carbon: Toward a very high surface area and hydrogen uptake. *J. Am. Chem. Soc.* **133**, 11854 (2011).
54. G. Ye, X. Zhu, S. Chen, D. Li, Y. Yin, Y. Lu, S. Komarneni, and D. Yang: Nanoscale engineering of nitrogen-doped carbon nanofiber aerogels for enhanced lithium ion storage. *J. Mater. Chem. A* **5**, 8247 (2017).
55. O.L. Li, S. Chiba, Y. Wada, G. Panomsuwan, and T. Ishizaki: Synthesis of graphitic-N and amino-N in nitrogen-doped carbon via a solution plasma process and exploration of their synergic effect for advanced oxygen reduction reaction. *J. Mater. Chem. A* **5**, 2073 (2017).
56. W. Tian, H. Zhang, H. Sun, M.O. Tadé, and S. Wang: Template-free synthesis of N-doped carbon with pillared-layered pores as bifunctional materials for supercapacitor and environmental applications. *Carbon* **118**, 98 (2017).
57. H. Jiang, P.S. Lee, and C. Li: 3D carbon based nanostructures for advanced supercapacitors. *Energy Environ. Sci.* **6**, 41 (2013).
58. B-H. Kim, K.S. Yang, and J.P. Ferraris: Highly conductive, mesoporous carbon nanofiber web as electrode material for high-performance supercapacitors. *Electrochim. Acta* **75**, 325 (2012).
59. W. Chaikittilip, M. Hu, H. Wang, H.S. Huang, T. Fujita, K.C. Wu, L.C. Chen, Y. Yamauchi, and K. Ariga: Nanoporous carbons through direct carbonization of a zeolitic imidazolate

- framework for supercapacitor electrodes. *Chem. Commun.* **48**, 7259 (2012).
60. P. Cheng, T. Li, H. Yu, L. Zhi, Z. Liu, and Z. Lei: Biomass-derived carbon fiber aerogel as a binder-free electrode for high-rate supercapacitors. *J. Phys. Chem. C* **120**, 2079 (2016).
 61. H. Jiang, C. Li, T. Sun, and J. Ma: A green and high energy density asymmetric supercapacitor based on ultrathin MnO₂ nanostructures and functional mesoporous carbon nanotube electrodes. *Nanoscale* **4**, 807 (2012).
 62. W. Xiong, M. Liu, L. Gan, Y. Lv, Y. Li, L. Yang, Z. Xu, Z. Hao, H. Liu, and L. Chen: A novel synthesis of mesoporous carbon microspheres for supercapacitor electrodes. *J. Power Sources* **196**, 10461 (2011).
 63. Q. Li, R. Jiang, Y. Dou, Z. Wu, T. Huang, D. Feng, J. Yang, A. Yu, and D. Zhao: Synthesis of mesoporous carbon spheres with a hierarchical pore structure for the electrochemical double-layer capacitor. *Carbon* **49**, 1248 (2011).
 64. D. Bhattacharjya, M-S. Kim, T-S. Bae, and J-S. Yu: High performance supercapacitor prepared from hollow mesoporous carbon capsules with hierarchical nanoarchitecture. *J. Power Sources* **244**, 799 (2013).
 65. D-D. Zhou, W-Y. Li, X-L. Dong, Y-G. Wang, C-X. Wang, and Y-Y. Xia: A nitrogen-doped ordered mesoporous carbon nanofiber array for supercapacitors. *J. Mater. Chem. A* **1**, 8488 (2013).
 66. H. Jiang, L. Yang, C. Li, C. Yan, P.S. Lee, and J. Ma: High-rate electrochemical capacitors from highly graphitic carbon-tipped manganese oxide/mesoporous carbon/manganese oxide hybrid nanowires. *Energy Environ. Sci.* **4**, 1813 (2011).
 67. M. Seredych and T.J. Bandoz: S-doped micro/mesoporous carbon-graphene composites as efficient supercapacitors in alkaline media. *J. Mater. Chem. A* **1**, 11717 (2013).
 68. Y. Lv, F. Zhang, Y. Dou, Y. Zhai, J. Wang, H. Liu, Y. Xia, B. Tu, and D. Zhao: A comprehensive study on KOH activation of ordered mesoporous carbons and their supercapacitor application. *J. Mater. Chem.* **22**, 93 (2012).
 69. Z. Lei, N. Christov, L.L. Zhang, and X.S. Zhao: Mesoporous carbon nanospheres with an excellent electrocapacitive performance. *J. Mater. Chem.* **21**, 2274 (2011).
 70. M. Li and J. Xue: Integrated synthesis of nitrogen-doped mesoporous carbon from melamine resins with superior performance in supercapacitors. *J. Phys. Chem. C* **118**, 2507 (2014).
 71. L. Sun, C. Tian, M. Li, X. Meng, L. Wang, R. Wang, J. Yin, and H. Fu: From coconut shell to porous graphene-like nanosheets for high-power supercapacitors. *J. Mater. Chem. A* **1**, 6462 (2013).
 72. J. Zhi, W. Zhao, X. Liu, A. Chen, Z. Liu, and F. Huang: Highly conductive ordered mesoporous carbon based electrodes decorated by 3D graphene and 1D silver nanowire for flexible supercapacitor. *Adv. Funct. Mater.* **24**, 2013 (2014).
 73. J.J. Cai, L.B. Kong, J. Zhang, Y.C. Luo, and L. Kang: A novel polyaniline/mesoporous carbon nano-composite electrode for asymmetric supercapacitor. *Chin. Chem. Lett.* **21**, 1509 (2010).
 74. Y-Y. Wang, B-H. Hou, H-Y. Lü, F. Wan, J. Wang, and X-L. Wu: Porous N-doped carbon material derived from prolific chitosan biomass as a high-performance electrode for energy storage. *RSC Adv.* **5**, 97427 (2015).
 75. J. Deng, T. Xiong, F. Xu, M. Li, C. Han, Y. Gong, H. Wang, and Y. Wang: Inspired by bread leavening: One-pot synthesis of hierarchically porous carbon for supercapacitors. *Green Chem.* **17**, 4053 (2015).
 76. L. Zhou, H. Cao, S. Zhu, L. Hou, and C. Yuan: Hierarchical micro-/mesoporous N- and O-enriched carbon derived from disposable cashmere: A competitive cost-effective material for high-performance electrochemical capacitors. *Green Chem.* **17**, 2373 (2015).

Supplementary Material

To view supplementary material for this article, please visit <https://doi.org/10.1557/jmr.2018.219>.